

Complex magnetism of B20-MnGe: from spin-spirals, hedgehogs to monopoles

Marcel Bornemann,* Sergii Grytsiuk, Paul F. Baumeister, Manuel dos Santos Dias, Rudolf Zeller, Samir Lounis,† and Stefan Blügel
*Peter Grünberg Institut and Institute for Advanced Simulation,
Forschungszentrum Jülich & JARA, 52425 Jülich, Germany*

B20 compounds are the playground for various non-trivial magnetic textures such as skyrmions, which are topologically protected states. Recent measurements on B20-MnGe indicate no clear consensus on its magnetic behavior, which is characterized by the presence of either spin-spirals or 3-dimensional objects interpreted to be a cubic lattice of hedgehogs and anti-hedgehogs. Utilizing a massively parallel linear scaling all-electron density functional algorithm, we find from full first-principles simulations on cells containing thousands of atoms that upon increase of the compound volume, the state with lowest energy switches across different magnetic phases: ferromagnetic, spin-spiral, hedgehog and monopole.

I. INTRODUCTION

Most of the current research activity dealing with magnetism in B20 compounds is closely connected to the field of skyrmionics. Skyrmions are two-dimensional non-trivial magnetization solitons¹⁻³, i.e. two-dimensional magnetic structures localized in space, of topological nature⁴, which have particle-like properties. Such magnetic objects are heavily prospected with the aim of establishing them as possible information-carrying particles that are small-sized and stable up to room temperature⁵⁻¹⁶. This motivated numerous studies on cubic B20-type compounds with broken lattice inversion symmetry^{4,17}, where skyrmion phases have been observed for the first time experimentally¹⁸. MnGe is a B20 compound that has been the subject of intense experimental and theoretical investigations, and yet there is still no consensus on how to explain its magnetic properties. The seminal work of Kanazawa et al.¹⁹ already showed that MnGe is rather intriguing. The magnetic structure was found to have a period between 3 and 6 nm, which is rather short in comparison to the other B20 compounds¹⁷, to be stable up to a temperature of 170 K and a magnetic field of 12 T, and to generate a strong topological Hall effect⁴. The magnetic structure of MnGe has been investigated in reciprocal space via neutron scattering¹⁹⁻³⁰, in real space via Lorentz transmission electron microscopy (LTEM)³⁰⁻³², and indirectly via transport experiments^{19,33-35}.

The canonical theory of helimagnetism in B20 compounds^{4,36,37} is based on a micromagnetic model featuring two main parameters: the exchange stiffness A and the spin-orbit-driven Dzyaloshinskii-Moriya interaction (or spiralization) D . Several theoretical works have calculated either D ³⁸⁻⁴¹ or both D and A ^{42,43} from density functional theory calculations, but the reported values are quite scattered. The main finding from these works is that D is too small when combined with A to explain the experimentally observed short period of the magnetic structure, which is given by $\lambda \approx 4\pi A/D$.

Experimentally, the magnetic structure has been interpreted as consisting of helical spirals^{21,25-27,29} as in

other B20 compounds, with the short period ascribed to competing long-range magnetic interactions^{26,29}. Transport signatures and LTEM imaging strongly back a more complex magnetic structure, which has initially been interpreted as a conventional two-dimensional skyrmion lattice^{19,20,31,33}, and afterwards as a three-dimensional skyrmion-antiskyrmion or hedgehog-antihedgehog lattice^{28,30,32,35}. Yaouanc and co-workers⁴⁴ analyzed muon spin resonance measurements⁴⁵ in favor of a helical spiral, and called for further theoretical work to clarify the issue of the magnetic structure of MnGe. Further evidence favoring the helical structure was provided by recent microwave absorption spectroscopy experiments⁴⁶.

In this article, we present results on B20-MnGe both from a magnetic model approach and large-scale all-electron calculations for a supercell whose extent compares to the periodicity of the experimentally observed helical textures. After discussing the electronic properties and analyzing the magnetic interactions obtained from the ferromagnetic unit cell, we explore various potential magnetic textures obtained from the self-consistent large-scale ab-initio simulations. The accuracy of the results are scrutinized in terms of convergence of the magnetic interactions as function of the interatomic distances and their sensitivity to various parameters. We found that the experimentally proposed hedgehog structures are marginally higher in energy than the ferromagnetic state around the experimental lattice parameters. Increasing the volume of the cell can lead to a stabilization of single spirals and of hedgehog lattice states. While possible disagreement with recent experiments can be blamed on the accuracy of the calculated electronic structure, our investigation calls for further studies on the three-dimensional magnetism in B20-MnGe.

II. METHODS

All of the results presented below are based on Density Functional Theory (DFT) calculations. We utilize the DFT codes juKKR^{47,48} and KKRnano⁴⁹ which are

both based on the Korringa-Kohn-Rostoker Green function formalism^{47,50}. The bilinear magnetic exchange interactions are obtained by infinitesimal rotations of the magnetic moments in the ferromagnetic state^{51–53}, which are implemented in juKKR following Ref. 53. KKRnano was especially designed to perform large-scale electronic structure calculations and allows us to perform self-consistent all-electron calculations for supercells that contain a few thousand atoms⁴⁹. The finite-temperature energy integration method of Wildberger et al. was used⁵⁴ with $T = 800$ K.

In section III, we review the basic electronic and magnetic properties of the primitive cell of B20-MnGe. To identify the appropriate exchange and correlation functional to utilize for the large supercells, we determine the theoretical equilibrium lattice parameter within the scalar-relativistic approximation as implemented in KKRnano. As exchange-correlation functionals, we choose the local density approximation (LDA) according to the spin-dependent scheme of Vosko, Wilk and Nusair⁵⁵, and the generalized gradient approximation as given in PBEsol⁵⁶. A grid of $14 \times 14 \times 14$ k-points is used.

In section IV, we perform first-principles calculations including spin-orbit coupling⁴⁸ with the juKKR code to extract the bilinear magnetic pair interactions between the Mn atoms in B20-MnGe, namely the isotropic exchange interactions (J_{ij}) and the Dzyaloshinskii-Moriya interactions (\vec{D}_{ij}). The k-point mesh was increased to $60 \times 60 \times 60$ points. Two kinds of calculations are performed: (i) at the theoretical PBEsol lattice parameter but displacing the internal positions of the Mn atoms, and (ii) keeping the internal positions of the Mn atoms fixed but varying the lattice parameter. Additionally, we use an in-house Monte-Carlo code that only considers the isotropic exchange interactions to determine the Curie temperature of the system using the Metropolis algorithm^{57,58}. We also performed atomistic spin dynamics simulations with the Spirit code⁵⁹, which are based on the numerical solution of the Landau-Lifshitz-Gilbert equation for a spin lattice model that takes into account all the computed bilinear magnetic interactions, and that can find the magnetic ground state and also metastable states.

For the large-scale calculations with KKRnano in section V we use supercells built of $6 \times 6 \times 6$ unit cells so that 1728 atoms are treated including spin-orbit coupling. PBEsol is used as exchange-correlation functional and only a single k -point, i.e. the Γ -point, is included. The Green function is truncated beyond a distance of $2a$. The magnetic states are imposed on the system by forcing the atomic exchange-correlation B-fields to point into specific directions.

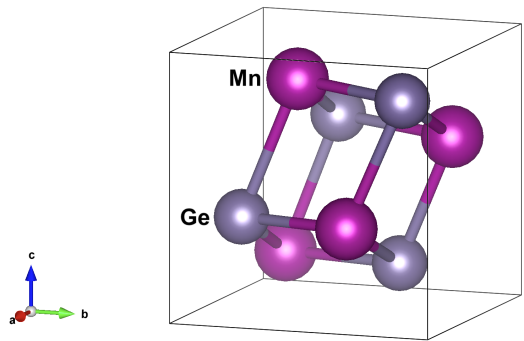


FIG. 1. Crystal structure of B20-MnGe. The four Mn atoms are equivalent, as are the four Ge atoms.

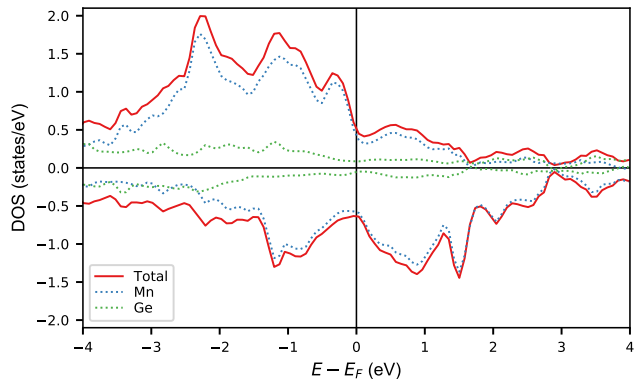


FIG. 2. Energy-resolved density of states for B20-MnGe. The contributions of the Mn bands and the Ge bands are plotted separately with dotted lines while the combined density of both the Mn and the Ge states is indicated by a solid line. The majority (minority) spin channel is denoted by positive (negative) y-values. The spin splitting, which gives rise to the magnetic moment of the Mn atoms, is clearly recognizable.

III. BASIC PROPERTIES OF FERROMAGNETIC B20-MnGe

B20-MnGe orders in a cubic structure that is described by the $P2_13$ space group. This space group is noncentrosymmetric, which means that there is no lattice inversion symmetry. The eight atoms in the primitive cell are located at the Wyckoff positions (u, u, u) , $(1/2 - u, 1 - u, 1/2 + u)$, $(1 - u, 1/2 + u, 1/2 - u)$ and $(1/2 + u, 1/2 - u, 1 - u)$, where u is a constant value that is determined for each atom type. We choose these parameters as $u_{\text{Mn}} = 0.135$ and $u_{\text{Ge}} = 0.8435$ which is in good agreement with experimental findings^{21,60,61}. The crystal structure is represented in Fig. 1.

We start by computing the basic electronic properties of the ferromagnetic 8-atom unit cell with the lattice parameter set to the experimental lattice parameter, $a = 4.79 \text{ \AA}$ ^{21,60,61}. In Fig. 2 the density of states obtained with KKRnano is shown. One recognizes the large spin-splitting characterizing Mn atoms, which gives rise to a

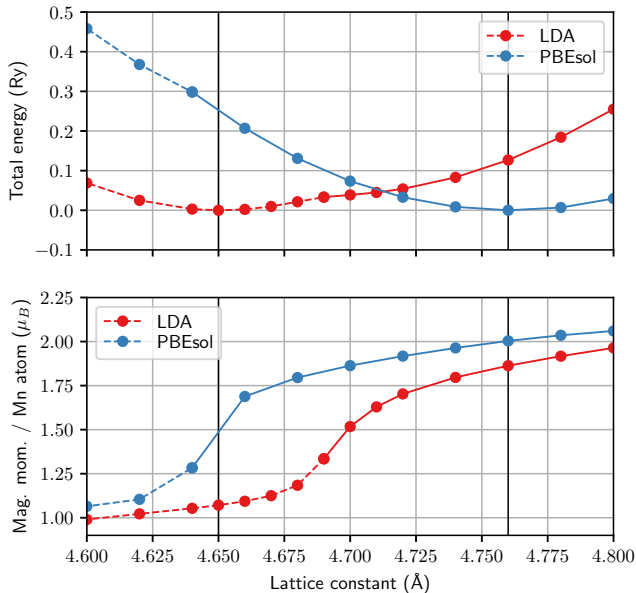


FIG. 3. Comparison of LDA and PBEsol exchange-correlation functionals for B20-MnGe. Top: Total energy vs. lattice parameter with LDA and PBEsol functionals. The equilibrium lattice constants for each functional are marked by two vertical black lines. The respective minimum energy is taken as energy zero for the corresponding total energy curve. Bottom: Magnetic moment per Mn atom vs. lattice parameter, showing a high-spin (large magnetic moment) to low-spin (small magnetic moment) transition for lattice compression.

magnetic moment of roughly $2\mu_B$ per Mn atom. The Ge states do not contribute significantly to the density of states at and around the Fermi level.

Next we explore how the magnetic moment depends on the assumed lattice constant. We recover the pressure-induced magnetic transition from a high-spin state (HS) to a low-spin (LS) state (see Fig. 3), i.e. a significant and rather abrupt reduction of the magnetic moment of Mn, that was predicted by Rößler⁶² and confirmed experimentally by Deutsch et al.²⁴. The latter reported additionally that the helical ordering in the material collapses above an applied pressure of 10 GPa.

The computed total energies as a function of the lattice parameter show that the LDA equilibrium lattice constant, $a = 4.65 \text{ \AA}$, is substantially lower than the PBEsol one, $a = 4.76 \text{ \AA}$, see Fig. 3, and that the latter is closer to the experimental value, $a = 4.79 \text{ \AA}$ ^{21,60,61}. The calculation also sheds light on the behavior of the magnetic moment under variation of the lattice constant. As can be seen in the lower part of Fig. 3, the magnetic moment of each Mn atom becomes larger with increasing lattice constant. The main difference between LDA and PBEsol is the location of the crossover region between the LS and HS state in which the moments increase abruptly and the system goes into the HS state. For PBEsol it is found around $a = 4.65 \text{ \AA}$ while it is slightly below $a = 4.7 \text{ \AA}$ for LDA. Furthermore, it is remarkable that

the magnetic moments per Mn atom differ a lot for the equilibrium lattice constant of LDA and PBEsol. Here, LDA predicts a magnetic moment per Mn atom that is a bit larger than $1\mu_B$, where instead PBEsol yields a value of almost $2\mu_B$. Experimentally, the magnetic moment was reported in the range $1.6 - 2.3\mu_B$ ^{19,21,24,25}. A closer look reveals that there are actually two parabola-like energy curves for each functional. One describes the total energy of the system in the HS state (solid line) while the other does the same for the LS state (dashed line). At the transition point the two curves intersect and the two states are degenerate.

To summarize, a HS/LS transition is predicted with both LDA and PBEsol, where PBEsol correctly finds the ground state to be the HS state while LDA does not, for the respective theoretical lattice parameters. As the PBEsol equilibrium lattice constant is also much closer to the experimental value, we restrict ourselves to PBEsol as exchange-correlation functional in the following.

IV. MAGNETIC EXCHANGE INTERACTIONS

The magnetic pair interactions are associated with the following extended Heisenberg model

$$E_{\text{atom}} = - \sum_{ij} J_{ij} \vec{m}_i \cdot \vec{m}_j + \sum_{ij} \vec{D}_{ij} \cdot (\vec{m}_i \times \vec{m}_j), \quad (1)$$

where \vec{m}_i is the unit vector for the orientation of the Mn magnetic moment at site i , J_{ij} is the isotropic exchange interaction and \vec{D}_{ij} is the vector characterizing the DMI, and both connect the moments on sites i and j . Since each Ge atom carries a small magnetic moment of $0.1\mu_B$, they are not considered in our magnetic models.

The canonical theory of helical magnetic structures in the B20 materials is based on the competition between the isotropic exchange interactions and the DMI^{4,36,37}. As the helical period in these materials tends to be much larger than the lattice parameter, this theory is conveniently expressed by a micromagnetic model where the energy reads

$$E_{\text{micro}} = \int dV [A ((\nabla m_x)^2 + (\nabla m_y)^2 + (\nabla m_z)^2) + D \vec{m} \cdot (\nabla \times \vec{m})], \quad (2)$$

where $\vec{m}(\vec{r})$ is the normalized magnetization field, A is the exchange stiffness, and D is the DM spiralization as already mentioned in the introduction. The period of the helical structure λ is then proportional to A/D and given by the provision

$$\lambda = \frac{2\pi}{q} = -4\pi \frac{A}{D}, \quad (3)$$

where q is the wave number. Note that this expression is only valid for the helical 1Q phase. In order to apply this theory to MnGe, the exchange stiffness A and the

DM spiralization D are evaluated from their respective interatomic counterparts, J_{ij} and \vec{D}_{ij} , respectively, by summation over all pairs of magnetic sites up to a chosen cutoff distance. The relation between the lattice and micromagnetic models is discussed in appendix A.

In this section, we first compute the magnetic pair interactions from the ferromagnetic state and then construct the micromagnetic parameters A and D .

A. Magnetic pair interactions

We investigate the sensitivity of the computed magnetic interactions to the structural parameters defining the unit cell in two ways. First, we keep the lattice parameter fixed at the theoretical PBEsol value, but vary the internal positions of the Mn atoms by setting $u_{\text{Mn}} = 0.125, 0.135$ and 0.145 (the positions of the Ge atoms are fixed). The computed J_{ij} and $|\vec{D}_{ij}|$ are shown in the top two plots of Fig. 4. We call each distinct interatomic separation between Mn atoms a shell. The first J_{ij} shell (nearest-neighbor interaction) is always large and positive, indicating strong ferromagnetic coupling. The next J_{ij} shells alternate in sign, which indicates magnetic frustration, and are more sensitive to the u -parameter. The values of $|\vec{D}_{ij}|$ are two orders of magnitude smaller than the values of J_{ij} , and shells other than the first also show sensitivity to the choice of u -parameter, as was the case for the isotropic interactions. We rationalize this behavior as follows: When the internal positions of the Mn atoms are varied, the distance between pairs of Mn and Ge atoms in the crystal structure changes. This modifies the hybridization between both atom types for certain pairs, which might be the reason for the found changes in the interactions.

Second, we keep the internal positions fixed ($u_{\text{Mn}} = 0.135$) and vary the lattice parameter. We consider only lattice expansion, as we expect that it might weaken the dominant nearest-neighbor ferromagnetic coupling, and so open the possibility of a different magnetic ground state. The values of J_{ij} and $|\vec{D}_{ij}|$ are shown in Fig. 5 for $a = 4.85, 4.90, 5.00$ and 5.10 \AA , which are all larger than the theoretical PBEsol lattice constant ($a = 4.76 \text{ \AA}$). As anticipated, the J_{ij} for the first shell are strongly reduced with increasing lattice parameter, while the ones for further shells are much less affected. The behavior of $|\vec{D}_{ij}|$ differs between the two smaller and the two larger lattice parameters. For $a = 4.85$ and 4.90 \AA , the $|\vec{D}_{ij}|$ for the first shell is the largest, while for $a = 5.00$ and 5.10 \AA it is strongly reduced while the $|\vec{D}_{ij}|$ for the fourth shell is strongly enhanced and now dominates over the one of the first shell.

B. Micromagnetic parameters

Now we turn to the micromagnetic spin stiffness A and DM spiralization D , which are defined in terms of their interatomic counterparts as explained in appendix A. The results are shown in the bottom panels of Fig. 4 and Fig. 5. The first observation is that the micromagnetic parameters do not converge with increased interatomic cutoff distance in the summations. This prevents us from evaluating the helical pitch λ by eq. (3), according to the canonical theory. Note that estimating the pitch in this manner is only valid if the magnetic texture is truly created by the competition of the spin stiffness and DM spiralization as given by the micromagnetic model. If frustration of the magnetic interactions plays a crucial role⁶³, this theory is no longer applicable. On the other hand, this poor convergence indicates that the underlying magnetic pair interactions are extremely long-ranged. This agrees with an alternative scenario for the origin of the magnetic ground state of MnGe, which is based on RKKY interactions^{26,29}.

Despite the lack of convergence of the summations, many conclusions can still be taken from studying the micromagnetic parameters. First we discuss the role played by varying the internal positions of the Mn atoms. As a function of the interatomic cutoff distance in the summations, the spin stiffness starts from fairly large values, dips at $\approx 0.9a$ due to antiferromagnetic J_{ij} (c.f. top left panel of Fig. 4), before plunging to fairly small ones when the cutoff exceeds $\approx 1.5a$ (see bottom left panel of Fig. 4). This is both an indication that interactions between far-away atoms are important, sustaining our claim that they are long-ranged, but also that the interactions have a competing nature, so that when they are summed up the resulting value is low. While the values of $|\vec{D}_{ij}|$ for the first shell were quite insensitive to changes in u_{Mn} , the same is not true for the micromagnetic D computed from those pairwise interactions (see first three data points on bottom right panel of Fig. 4). This results from the progressive rotation of the DMI vectors \vec{D}_{ij} with respect to the bond vector connecting the two Mn atoms, which is central to the formula in eq. (A9) that defines D , and explains why the value of D changes from positive to near-zero to negative as u_{Mn} increases. This decrease of D when u_{Mn} increases is actually a general trend, as seen by the relative ordering of the three computed curves.

Next we discuss the impact of expanding the lattice on the micromagnetic parameters. As a function of the cutoff distance in the summations, the spin stiffness initially follows the same trend as the first shell of the J_{ij} , weakening as the lattice parameter is increased (see the bottom panel of Fig. 5). There is a strong dip at $\approx 0.9a$ due to antiferromagnetic J_{ij} (c.f. top left panel of Fig. 5), but then A increases again to a large positive value. Strikingly, an abrupt change once again takes place when the cutoff exceeds $\approx 1.5a$: A becomes negative, and its trend is to become more negative the more the lattice is ex-

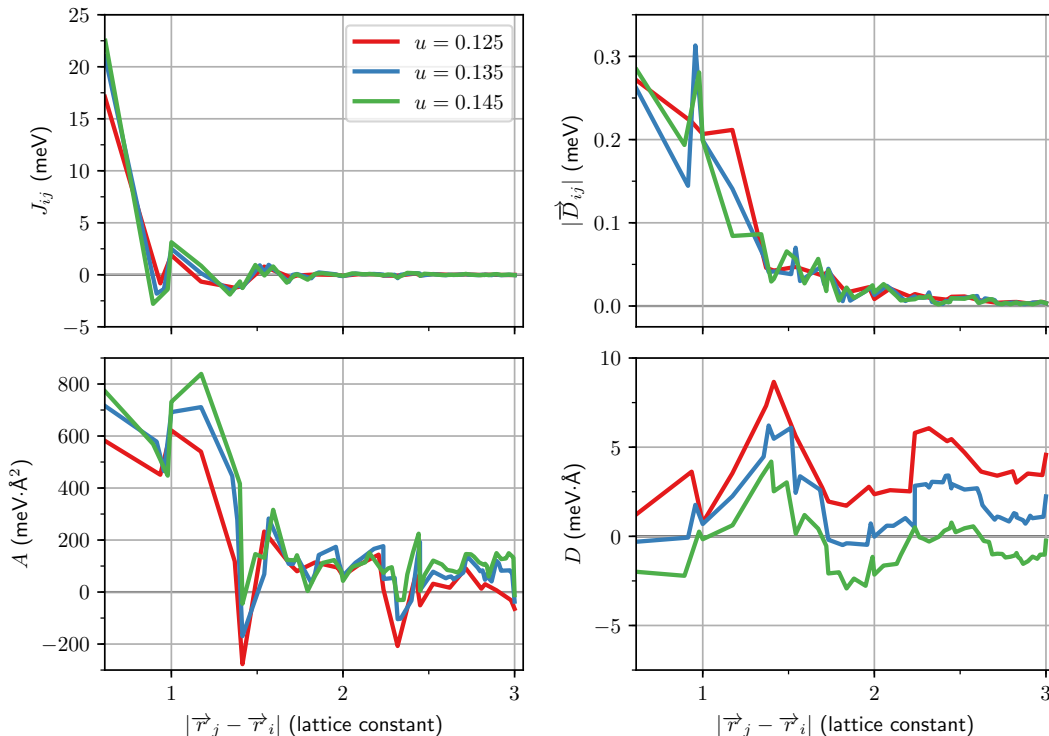


FIG. 4. Dependence of the magnetic interactions on the interatomic distance between Mn atoms when the internal Mn positions are varied. The *ab initio* calculations were performed with the juKKR code using the PBEsol functional at its theoretical lattice parameter, $a = 4.76 \text{ \AA}$. The internal positions of the Mn atoms were varied by setting $u_{\text{Mn}} = 0.125, 0.135$ and 0.145 . Top panels: isotropic magnetic exchange couplings J_{ij} and absolute values of the DMI vectors $|\vec{D}_{ij}|$ as a function of the interatomic distance between Mn atoms. Bottom panels: micromagnetic spin stiffness A and micromagnetic DM spiralization D computed from the magnetic pair interactions by summation up to the given interatomic distance. A and D do not converge to a constant value with the inclusion of further shells in the summations.

panded. The trigger is another shell of strong antiferromagnetic J_{ij} , but the remaining long-range part of the pair interactions does not seem to have a definite sign, so the overall negative tendency remains for larger cutoff distances. A negative spin stiffness immediately invalidates the assumptions behind the micromagnetic model of eq. (2), namely that the interactions are dominantly ferromagnetic, and so $A > 0$. This could be a hint to the existence of a helical magnetic texture driven by competing isotropic exchange interactions, instead of DMI. The spiralization tensor also shows a strong evolution with increasing lattice parameter. Starting again from the first shell of \vec{D}_{ij} , we already found that when the lattice parameter increases their magnitude decreases, but the micromagnetic D has a completely different behavior, first staying at fairly low values before increasing drastically for the largest lattice parameter considered, due to a realignment of the \vec{D}_{ij} with the bond vectors connecting the atoms. Increasing the cutoff distance in the summations does not produce any discernible trend in the behavior of D , though.

We close the discussion of the micromagnetic parameters by placing our results in the context of previous works on MnGe. Informed by the canonical micromag-

netic theory, most attention has focused on the D parameter. An approach by Koretsune et al. based on taking the limit of the static non-uniform spin susceptibility constructed from a Wannier representation resulted in the value $D = 107 \text{ meV \AA}^{38}$, with a revised value of $D \approx 27 \text{ meV \AA}$ computed by the same method being reported in a recent review³⁹. Different approaches, based on the DFT energies of spin spirals or a different derivation of the spiralization tensor, resulted in the values $D = 1.2 \text{ meV \AA}^{42}$, $D \approx -1.8 \text{ meV \AA}^{43}$, and $D \approx 1 \text{ meV \AA}^{40,41}$. We see that the literature consensus is for a small value of D , of the order of magnitude of the values we report on the bottom right panel of Fig. 4, with the results of the susceptibility method unexplained outliers. There seems to be less interest in the literature regarding the spin stiffness, with only two reported values: $A = 280 \text{ meV \AA}^{42}$ and $A \approx 800 \text{ meV \AA}^{43}$. The first value is an upper bound for our computed stiffness at large cutoff distances, while the second value is similar to our computed stiffness from the first couple of shells of J_{ij} interactions, see bottom left panel of Fig. 4.

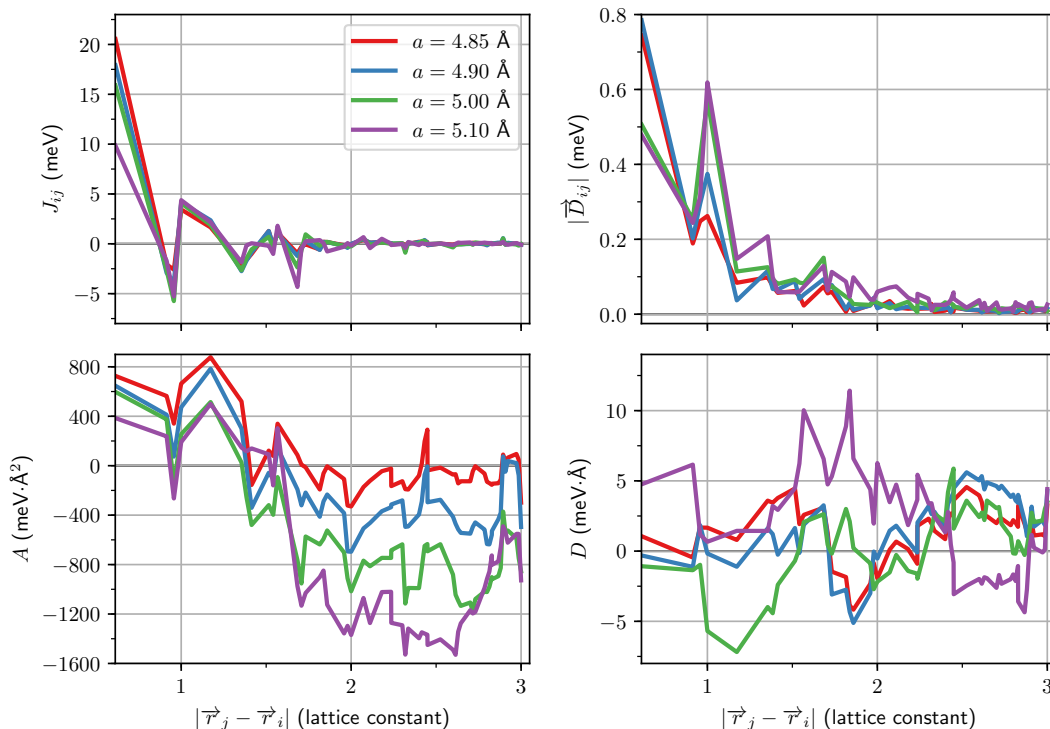


FIG. 5. Dependence of the magnetic interactions on the interatomic distance between Mn atoms when the lattice parameter is varied. The *ab initio* calculations were performed with the juKKR code using the PBEsol functional at fixed $u_{\text{Mn}} = 0.135$. The lattice parameters were set to $a = 4.85, 4.90, 5.00$ and 5.10 Å. Top panels: isotropic magnetic exchange couplings J_{ij} and absolute values of the DMI vectors $|\vec{D}_{ij}|$ as a function of the interatomic distance between Mn atoms. Bottom panels: micromagnetic spin stiffness A and micromagnetic DM spiralization D computed from the magnetic pair interactions by summation up to the given interatomic distance. A and D do not converge to a constant value with the inclusion of further shells in the summations.

C. Atomistic spin dynamics

The preceding analysis of the trends and properties of the micromagnetic parameters raised some doubts on whether the canonical theory based on the micromagnetic model is the right approach to describe the magnetism of MnGe. However, we can revert to the lattice spin model of eq. (1) and explore its output.

We return to the isotropic pair interactions, J_{ij} , and use a Monte Carlo approach to estimate the Curie temperature as a function of the range of the considered interactions. In this way we can ascertain if the long-ranged nature of these interactions impacts this finite-temperature property. As a test case, we choose the $u_{\text{Mn}} = 0.135$ case at the theoretical PBEsol lattice parameter. The results of the Monte Carlo simulations are shown in Fig. 6. We find that, although there is a dependence on the number of shells included in the simulations, T_C is more or less converged when interactions up to $2a$ are taken into account, in stark contrast to the micromagnetic parameters A and D . This converged value of $T_C \approx 300$ K lies above the experimental value $T_C^{\text{exp}} \approx 170$ K²⁰.

We used the complete set of pair interactions from the

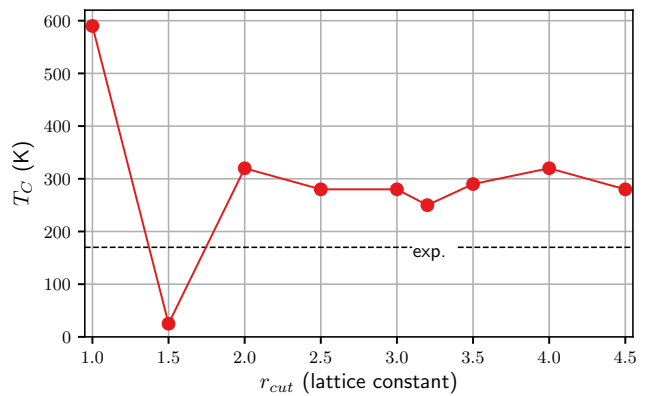


FIG. 6. Cutoff distance dependence of the Curie temperature T_C of B20-MnGe obtained with a Monte Carlo method. The isotropic exchange interactions J_{ij} from Fig. 4 for $u_{\text{Mn}} = 0.135$ at the theoretical PBEsol lattice parameter were used.

previously mentioned dataset, i.e. J_{ij} and \vec{D}_{ij} , to explore possible magnetic configurations in the lattice spin model. The atomistic spin dynamics carried out with the Spirit code uncovered the ferromagnetic state as the only

stable magnetic structure in 3D simulations, while we could also find metastable skyrmion-like textures when considering thin 2D slabs. Other than possible numerical difficulties arising from the long-ranged nature of the interactions, the failure of the simulations in finding a stable non-ferromagnetic state in 3D could mean that a model based on bilinear magnetic interactions is insufficient, and that more complex interactions (see e.g.⁶⁴) play an important role, as proposed in a recent work⁶⁵. As the first-principles DFT simulations implicitly account for all possible magnetic interactions based on the electronic structure, we next settle whether such non-ferromagnetic structure can be stabilized by performing the appropriate calculations on large supercells of MnGe.

V. LARGE-SCALE ELECTRONIC STRUCTURE CALCULATIONS WITH KKRnano

In this section, we present the large-scale DFT results that we obtained with KKRnano for B20-MnGe. We set up a supercell consisting of $6 \times 6 \times 6$ conventional unit cells (1728 atoms), which can describe features on a length scale of $6a \approx 3$ nm, the magnetic periodicity found experimentally^{19,20,22,23,26,28-32,35}. Besides the previously suggested non-trivial magnetic states, the helical spiral (1Q state) and the hedgehog lattice (3Q state), we explored the possibility of stabilizing the Bloch point (BP) state. These magnetic structures are illustrated in Fig. 7.

In our study, the lattice constant is varied and the total energies corresponding to the three states are tracked with respect to the ferromagnetic phase. As mentioned in the introduction, the main reason that motivates the usage of KKRnano in conjunction with B20-MnGe is that Tanigaki et al. reported on the existence of the 3Q hedgehog lattice state in this material³². Findings by Kanazawa et al. suggest that this lattice is set up by a superposition of three orthogonal helical structures also referred to as 3Q state¹⁷. Here, the magnetization is determined by the provision

$$\vec{M}(\vec{r}) = \begin{pmatrix} \sin qy + \cos qz \\ \sin qz + \cos qx \\ \sin qx + \cos qy \end{pmatrix}, \quad (4)$$

where $q = \frac{2\pi}{\lambda}$ is the wavenumber given in terms of the helical wavelength λ and x , y and z are the spatial coordinates within the unit cell. Note, that $\vec{M}(\vec{r})$ is not normalized. Equation (4) describes an alternating pattern of hedgehog and anti-hedgehog textures.

An illustration of an anti-hedgehog is given in Fig. 7 b). Following the micromagnetic description, singularities in the magnetization are expected within the magnetic texture⁶⁶. Our ab initio simulations indicate, however, that all atomic magnetic moments are finite, although our method does not prevent the occurrence of a fully quenched magnetization density within or in between atoms. In contrast to other systems exhibiting a

similar magnetic phase, the rather short helical wavelength of 3 to 6 nm in B20-MnGe allows one to perform density functional theory (DFT) calculations with KKRnano.

Other works^{21,25-27,29,44} propose that in B20-MnGe a helical spin spiral forms along the (001) direction where the magnetization is described by the relation

$$\vec{M}(\vec{r}) = \begin{pmatrix} \cos qz \\ -\sin qz \\ 0 \end{pmatrix}. \quad (5)$$

In the following, we refer to this as the 1Q state (see Fig. 7 a)).

Based on our findings in section IV, where we encounter a DM spiralization that does not seem to be larger than 10 meV Å, we also consider a magnetic configuration which can exist without a large DM spiralization but could yield transmission electron microscopy stripe contrasts similar to the 3Q state. An obvious candidate for this is a Bloch point texture which can be conveniently defined by means of the four spherical parameters ϕ , θ , Φ and Θ . The parameters ϕ and θ designate the position of an *individual atom* in the unit cell which is described by the common polar and azimuthal angle

$$\phi = \arctan(y/x) \quad (6)$$

and

$$\theta = \arccos\left(\frac{z}{\sqrt{x^2 + y^2 + z^2}}\right). \quad (7)$$

Usually, the atomic positions are given in the Cartesian coordinates x , y and z . In the definition above, we define the origin of the coordinate system, i.e. the tuple $(x = 0, y = 0, z = 0)$, to be at the center of the unit cell. In this frame of reference, all atoms that lay in an x-y-plane that intersects with the center are described by $\theta = \pi/2$. The orientation of the *individual atomic magnetic moments* for a BP texture is then defined by the polar angle

$$\Phi = \phi + \phi_1 \quad (8)$$

and the azimuthal angle

$$\Theta = 2 \arctan\left(\cot \frac{\theta}{2}\right), \quad (9)$$

where the angles designating the atomic position enter as arguments. The phase factor is set to $\phi_1 = \pi$, hence all magnetic moments point at the origin of the coordinate system. An illustration of this configuration is given in Fig. 7 c).

Since the lattice parameter of a material can be modified via strain that originates from the manufacturing process of the sample, we investigated the dependence of B20-MnGe's magnetic properties as function of volume. Such a dependence is depicted in the upper part

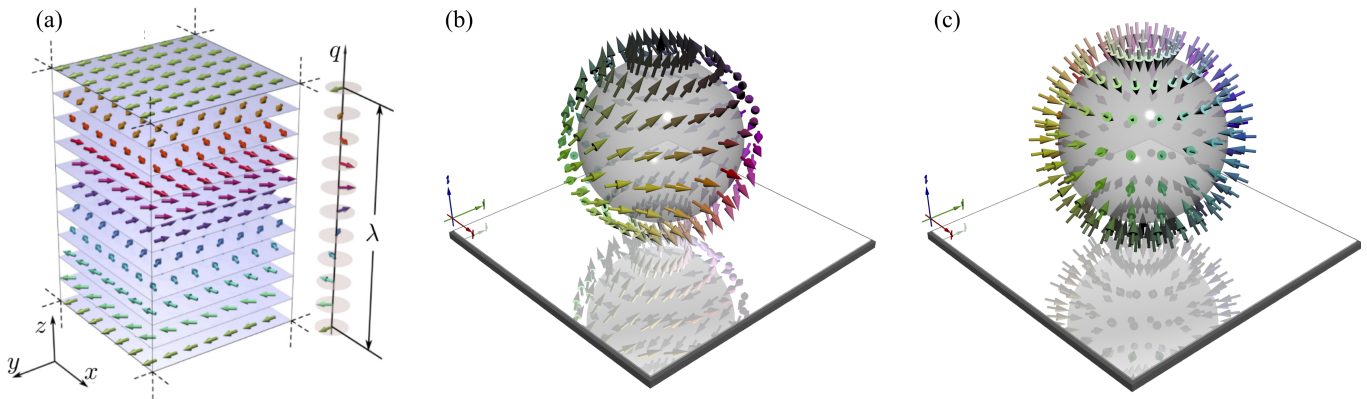


FIG. 7. Illustrations of magnetic textures that potentially exist in B20-MnGe: (a) Helical spin spiral that propagates in (001) direction. (b) Magnetic anti-hedgehog texture that is wrapped around a singularity at the center as it would exist in a 3Q hedgehog-antihedgehog lattice. (c) A Bloch point texture where all spins point into the center, thereby creating a monopole.

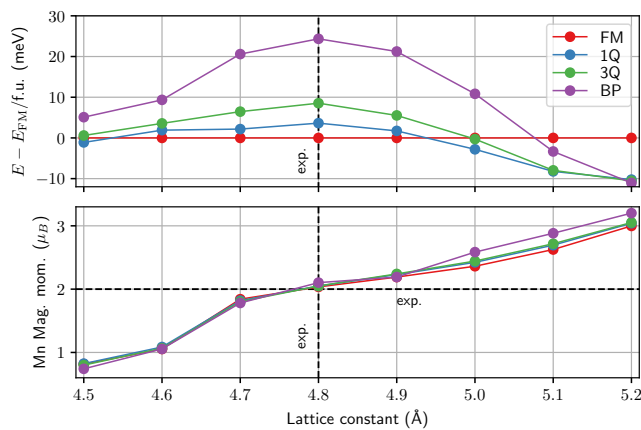


FIG. 8. Comparison of Ferromagnetic (FM), helical spiral (1Q), hedgehog lattice (3Q) and Bloch Point (BP) state in B20-MnGe with `KKRnano`. Top: Difference of total energies with the FM state as reference state for different lattice constants. The experimental lattice constant is $a = 4.80$ Å. Bottom: Magnetic moment per Mn atom increases with lattice constant. High-spin/Low-spin transition is clearly visible between $a = 4.60$ Å and $a = 4.70$ Å. Experimentally, the magnetic moment is measured to be $\approx 2\mu_B$.

of Fig. 8, where the total energy is evaluated for FM, 1Q, 3Q and BP states. The FM state constitutes the ground state, when the experimental lattice constant is assumed. However, 1Q and 3Q states are energetically not far from the FM state (within less than 10 meV per Mn atom). When we further increase the lattice constant the picture changes. A crucial transition point is found around $a = 5.0$ Å, where by imposing the 1Q or 3Q state the energy can be made lower than that of the ferromagnetic state. In general, for $a > 5.0$ Å 1Q and 3Q states are favored over the ferromagnetic one. The BP state is energetically not preferred for any lattice constant except for the rather large $a = 5.2$ Å.

In the lower part of Fig. 8 the evolution of the mag-

netic moment with varying lattice constant is tracked. The resulting magnetic moment for the experimental lattice constant nicely falls on top of the magnetic moment of approximately $2\mu_B$ per Mn atom which is reported experimentally^{21,23,24,44}. The HS/LS transition that is already shown in Fig. 3 is recognizable between $a = 4.60$ Å and $a = 4.70$ Å. Furthermore, the magnetic moment increases, when the lattice constant is increased. This is a common behavior which is often observed in metallic systems. For larger lattice constants the magnetic moments of the different magnetic textures differ more than for the smaller lattice constants.

VI. CONCLUSIONS

We investigated the magnetic properties of B20-MnGe through ab initio calculations. First we considered the basic properties of the ferromagnetic unit cell, recovering the already-known pressure-induced transition from a high-spin to a low-spin state. Then we analyzed the magnetic interactions derived from the first-principles calculations with both lattice and micromagnetic models. Lastly, we performed large-scale electronic structure calculations with `KKRnano` to quantify the relative energetic stability of different candidate magnetic structures, 1Q (helical spiral), 3Q (hedgehog-antihedgehog lattice) and BP (Bloch point) state, in relation to the ferromagnetic state. Both the magnetic model simulations and the supercell first-principles calculations found the ferromagnetic state to be the most stable state at the experimental lattice parameter, which is quite close to the theoretically determined one with `PBESol`. This is in clear contradiction with all reported experimental results.

The computed magnetic pair interactions showed that the isotropic exchange interactions J_{ij} are very long-ranged and alternate between ferro- and antiferromagnetic as a function of distance, while the Dzyaloshinskii-Moriya interactions \vec{D}_{ij} are rather weak in relation to

the former. This is theoretical evidence for the competing long-range magnetic interactions scenario proposed to explain the short period of the magnetic structure^{26,29}. The long-range nature of the magnetic interactions was evidenced by the difficulties found in converging the micromagnetic parameters A (exchange stiffness) and D (spiralization) that can be constructed by performing real-space summations over the corresponding pair interactions. Nevertheless, the trends in the micromagnetic parameters are in good correspondence with previous theoretical works^{40–43}. We envision two scenarios that could explain the experimental findings considering only pair interactions, both invoking competing exchange interactions: (i) $A \approx 0$, so that a weak D can stabilize helical modulations; (ii) $A < 0$, signaling the instability of the ferromagnetic state to helical modulations, with D playing a secondary role of selecting the chirality of the modulation.

The first-principles calculations performed for the ferromagnetic, 1Q, 3Q and Bloch point structures found that it is possible to stabilize either the 1Q or the 3Q structures with respect to the ferromagnetic state if the lattice parameter is increased. This can be interpreted by the computed magnetic pair interactions, which showed a change in sign of A due to a weakening of the ferromagnetic nearest-neighbor J_{ij} , and a strengthening of D due to a rotation of the \vec{D}_{ij} towards the bond directions, which more than compensates the reduction in their magnitudes. Overall, the energy differences between the 1Q and 3Q structures and the ferromagnetic state was at most 10 meV per Mn atom, which is a model-independent verification that the magnetic interactions in the system are indeed competing, so that quite different magnetic structures have very similar energies. Regarding the Bloch point structure, the imposition of periodic boundary conditions in `KKRnano` means that the magnetic spins at the boundaries of each supercell are aligned in an unfavorable antiferromagnetic way and thus there is a large energy penalty. Notably, this energy cost decreases by increasing the lattice parameter, which can again be related to the reduction of the nearest-neighbor J_{ij} .

As all our results are based on first-principles calculations, a possible explanation for the disagreement with

experiment could be in the computed electronic structure. First, the small energy differences found for the supercell calculations might make the results sensitive to intrinsic deficiencies of the exchange-correlation functional. Second, and perhaps more likely, could be an excessive delocalization of the Mn d -orbitals. This is a well-known common failure of the standard functionals, which could upset the energetic balance between the different magnetic structures by strengthening the nearest-neighbor J_{ij} . The work reported in Ref.⁶⁷ could be interpreted in this way, and the authors do find several noncollinear magnetic structures by tuning the coupling between itinerant and more localized electrons.

Experimentally, it is not possible to have the ideal lattice structures considered in our study. Thus various effects can affect the experimental observations and the related interpretations. For instance, impurities in the sample can potentially exert chemical pressure, which leads to spatial expansion of the lattice structure (see the example of Co-doped B20-FeGe⁶⁸). Overall our study motivates further theoretical and experimental investigations of three-dimensional magnetism in B20 materials in general and in B20-MnGe in particular.

ACKNOWLEDGEMENTS

We thank Nikolai S. Kiselev for fruitful discussions. We acknowledge funding from Deutsche Forschungsgemeinschaft (DFG) through SPP 2137 “Skyrmionics”, the Collaborative Research Centers SFB 1238 and SFB/TRR 173. S.B. acknowledges the DARPA TEE program through grant MIPR# HR0011831554 from DOI. S.L. and M.d.S.D. acknowledge support from the European Research Council (ERC) under the European Union’s Horizon 2020 research and innovation program (ERC-consolidator grant 681405 – DYNASORE). We gratefully acknowledge the Gauss Centre for Supercomputing e.V. (www.gauss-centre.eu) for funding this project by providing computing time through the project GCS-KKRn on the GCS Supercomputer Hazel Hen at Hchstleistungsrechenzentrum Stuttgart (HLRS). We further acknowledge Forschungszentrum Jlich/Jlich Supercomputing Centre for granting access to the QPACE 3 computer, which was built as part of the DFG (SFB/TRR 55) project.

* m.bornemann@fz-juelich.de

† s.lounis@fz-juelich.de

¹ A. N. Bogdanov and D. Yablonskii, *J. Exp. Theor. Phys.* **95**, 178 (1989).

² U. K. Rler, A. N. Bogdanov, and C. Pfeleiderer, *Nature* **442**, 797 (2006).

³ K. Everschor-Sitte, J. Masell, R. M. Reeve, and M. Klui, *Journal of Applied Physics* **124**, 240901 (2018).

⁴ N. Nagaosa and Y. Tokura, *Nature Nanotechnology* **8**, 899 (2013).

⁵ A. Fert, V. Cros, and J. Sampaio, *Nature Nanotechnology* **8**, 152 (2013).

⁶ R. Tomasello, E. Martinez, R. Zivieri, L. Torres, M. Carpentieri, and G. Finocchio, *Scientific Reports* **4**, 6784 (2014).

⁷ D. M. Crum, M. Bouhassoune, J. Bouaziz, B. Schweflinghaus, S. Blügel, and S. Lounis, *Nature Commun.* **6**, 8541

- (2015).
- ⁸ G. Finocchio, M. Ricci, R. Tomasello, A. Giordano, M. Lanuzza, V. Puliafito, P. Burrascano, B. Azzerboni, and M. Carpentieri, *Applied Physics Letters* **107**, 262401 (2015).
 - ⁹ X. Zhang, Y. Zhou, M. Ezawa, G. Zhao, and W. Zhao, *Scientific Reports* **5**, 11369 (2015).
 - ¹⁰ M. dos Santos Dias, J. Bouaziz, M. Bouhassoune, S. Blügel, and S. Lounis, *Nature Commun.* **7**, 13613 (2016).
 - ¹¹ M. Mruczkiewicz, P. Gruszecki, M. Zelent, and M. Krawczyk, *Phys. Rev. B* **93**, 174429 (2016).
 - ¹² A. Fert, N. Reyren, and V. Cros, *Nature Reviews Materials* **2**, 17031 (2017).
 - ¹³ F. Bttner, I. Lemesh, and G. S. D. Beach, *Scientific Reports* **8**, 4464 (2018).
 - ¹⁴ M. Leroux, M. J. Stolt, S. Jin, D. V. Pete, C. Reichhardt, and B. Maiorov, *Scientific Reports* **8**, 15510 (2018).
 - ¹⁵ I. Lima Fernandes, J. Bouaziz, S. Blügel, and S. Lounis, *Nat. Commun.* **9**, 4395 (2018).
 - ¹⁶ F. J. dos Santos, M. dos Santos Dias, F. S. M. Guimarães, J. Bouaziz, and S. Lounis, *Phys. Rev. B* **97**, 024431 (2018).
 - ¹⁷ N. Kanazawa, S. Seki, and Y. Tokura, *Advanced Materials* **29**, 1603227 (2017).
 - ¹⁸ S. Mhlbauer, B. Binz, F. Jonietz, C. Pfleiderer, A. Rosch, A. Neubauer, R. Georgii, and P. Boni, *Science* **323**, 915 (2009).
 - ¹⁹ N. Kanazawa, Y. Onose, T. Arima, D. Okuyama, K. Ohoyama, S. Wakimoto, K. Kakurai, S. Ishiwata, and Y. Tokura, *Physical Review Letters* **106**, 156603 (2011).
 - ²⁰ N. Kanazawa, J.-H. Kim, D. S. Inosov, J. S. White, N. Egetenmeyer, J. L. Gavilano, S. Ishiwata, Y. Onose, T. Arima, B. Keimer, and Y. Tokura, *Physical Review B* **86**, 134425 (2012).
 - ²¹ O. L. Makarova, A. V. Tsvyashchenko, G. Andre, F. Porcher, L. N. Fomicheva, N. Rey, and I. Mirebeau, *Physical Review B* **85**, 205205 (2012).
 - ²² S. V. Grigoriev, N. M. Potapova, S.-A. Siegfried, V. A. Dyadkin, E. V. Moskvina, V. Dmitriev, D. Menzel, C. D. Dewhurst, D. Chernyshov, R. A. Sadykov, L. N. Fomicheva, and A. V. Tsvyashchenko, *Physical Review Letters* **110**, 207201 (2013).
 - ²³ E. Altynbaev, S.-A. Siegfried, V. Dyadkin, E. Moskvina, D. Menzel, A. Heinemann, C. Dewhurst, L. Fomicheva, A. Tsvyashchenko, and S. Grigoriev, *Phys. Rev. B* **90**, 174420 (2014).
 - ²⁴ M. Deutsch, O. L. Makarova, T. C. Hansen, M. T. Fernandez-Diaz, V. A. Sidorov, A. V. Tsvyashchenko, L. N. Fomicheva, F. Porcher, S. Petit, K. Koepnik, U. K. Rler, and I. Mirebeau, *Physical Review B* **89**, 180407(R) (2014).
 - ²⁵ M. Deutsch, P. Bonville, A. V. Tsvyashchenko, L. N. Fomicheva, F. Porcher, F. Damay, S. Petit, and I. Mirebeau, *Phys. Rev. B* **90**, 144401 (2014).
 - ²⁶ E. Altynbaev, S.-A. Siegfried, E. Moskvina, D. Menzel, C. Dewhurst, A. Heinemann, A. Feoktystov, L. Fomicheva, A. Tsvyashchenko, and S. Grigoriev, *Physical Review B* **94**, 174403 (2016).
 - ²⁷ N. Martin, M. Deutsch, G. Chaboussant, F. Damay, P. Bonville, L. N. Fomicheva, A. V. Tsvyashchenko, U. K. Rössler, and I. Mirebeau, *Phys. Rev. B* **96**, 020413 (2017).
 - ²⁸ N. Kanazawa, J. S. White, H. M. Rnnow, C. D. Dewhurst, D. Morikawa, K. Shibata, T. Arima, F. Kagawa, A. Tsukazaki, Y. Kozuka, M. Ichikawa, M. Kawasaki, and Y. Tokura, *Physical Review B* **96**, 220414(R) (2017).
 - ²⁹ E. Altynbaev, S.-A. Siegfried, P. Strauß, D. Menzel, A. Heinemann, L. Fomicheva, A. Tsvyashchenko, and S. Grigoriev, *Phys. Rev. B* **97**, 144411 (2018).
 - ³⁰ Y. Fujishiro, N. Kanazawa, T. Nakajima, X. Z. Yu, K. Ohishi, Y. Kawamura, K. Kakurai, T. Arima, H. Mitamura, A. Miyake, K. Akiba, M. Tokunaga, A. Matsuo, K. Kindo, T. Koretsune, R. Arita, and Y. Tokura, *Nature Communications* **10**, 1059 (2019).
 - ³¹ K. Shibata, X. Z. Yu, T. Hara, D. Morikawa, N. Kanazawa, K. Kimoto, S. Ishiwata, Y. Matsui, and Y. Tokura, *Nature Nanotechnology* **8**, 723 (2013).
 - ³² T. Tanigaki, K. Shibata, N. Kanazawa, X. Yu, Y. Onose, H. S. Park, D. Shindo, and Y. Tokura, *Nano Letters* **15**, 5438 (2015).
 - ³³ Y. Shiomi, N. Kanazawa, K. Shibata, Y. Onose, and Y. Tokura, *Phys. Rev. B* **88**, 064409 (2013).
 - ³⁴ N. Kanazawa, K. Shibata, and Y. Tokura, *New Journal of Physics* **18**, 045006 (2016).
 - ³⁵ N. Kanazawa, Y. Nii, X. X. Zhang, A. S. Mishchenko, G. De Filippis, F. Kagawa, Y. Iwasa, N. Nagaosa, and Y. Tokura, *Nature Communications* **7**, 11622 (2016).
 - ³⁶ O. Nakanishi, A. Yanase, A. Hasegawa, and M. Kataoka, *Solid State Communications* **35**, 995 (1980).
 - ³⁷ P. Bak and M. H. Jensen, *Journal of Physics C: Solid State Physics* **13**, L881 (1980).
 - ³⁸ T. Koretsune, N. Nagaosa, and R. Arita, *Scientific Reports* **5**, 13302 (2015).
 - ³⁹ T. Koretsune, T. Kikuchi, and R. Arita, *Journal of the Physical Society of Japan* **87**, 041011 (2018).
 - ⁴⁰ S. Mankovsky, S. Wimmer, S. Polesya, and H. Ebert, *Physical Review B* **97**, 024403 (2018).
 - ⁴¹ S. Mankovsky, S. Polesya, and H. Ebert, *Phys. Rev. B* **99**, 104427 (2019).
 - ⁴² J. Gayles, F. Freimuth, T. Schena, G. Lani, P. Mavropoulos, R. A. Duine, S. Blgel, J. Sinova, and Y. Mokrousov, *Physical Review Letters* **115**, 036602 (2015).
 - ⁴³ T. Kikuchi, T. Koretsune, R. Arita, and G. Tatara, *Physical Review Letters* **116**, 247201 (2016).
 - ⁴⁴ A. Yaouanc, P. Dalmas de Rotier, A. Maisuradze, and B. Roessli, *Physical Review B* **95**, 174422 (2017).
 - ⁴⁵ N. Martin, M. Deutsch, F. Bert, D. Andreica, A. Amato, P. Bonf, R. De Renzi, U. K. Rler, P. Bonville, L. N. Fomicheva, A. V. Tsvyashchenko, and I. Mirebeau, *Physical Review B* **93**, 174405 (2016).
 - ⁴⁶ E. Turgut, H. Paik, K. Nguyen, D. A. Muller, D. G. Schlom, and G. D. Fuchs, *Phys. Rev. Materials* **2**, 074404 (2018).
 - ⁴⁷ N. Papanikolaou, R. Zeller, and P. H. Dederichs, *Journal of Physics: Condensed Matter* **14**, 2799 (2002).
 - ⁴⁸ D. S. G. Bauer, *Development of a relativistic full-potential first-principles multiple scattering Green function method applied to complex magnetic textures of nano structures at surfaces*, Schriften des Forschungszentrums Jlich Reihe Schlseltechnologien No. 79 (Forschungszentrum Jlich, Jlich, 2014).
 - ⁴⁹ A. Thiess, R. Zeller, M. Bolten, P. H. Dederichs, and S. Blgel, *Physical Review B* **85**, 235103 (2012).
 - ⁵⁰ H. Ebert, D. Ködderitzsch, and J. Minár, *Rep. Prog. Phys.* **74**, 096501 (2011).
 - ⁵¹ A. Liechtenstein, M. Katsnelson, V. Antropov, and V. Gubanov, *Journal of Magnetism and Magnetic Materials* **67**, 65 (1987).
 - ⁵² L. Udvardi, L. Szunyogh, K. Palots, and P. Weinberger, *Physical Review B* **68**, 104436 (2003).

- ⁵³ H. Ebert and S. Mankovsky, Physical Review B **79**, 045209 (2009).
- ⁵⁴ K. Wildberger, P. Lang, R. Zeller, and P. H. Dederichs, Physical Review B **52**, 11502 (1995).
- ⁵⁵ S. H. Vosko, L. Wilk, and M. Nusair, Canadian Journal of Physics **58**, 1200 (1980).
- ⁵⁶ J. P. Perdew, A. Ruzsinszky, G. I. Csonka, O. A. Vydrov, G. E. Scuseria, L. A. Constantin, X. Zhou, and K. Burke, Physical Review Letters **100**, 136406 (2008).
- ⁵⁷ M. Ležaić, P. Mavropoulos, G. Bihlmayer, and S. Blügel, Phys. Rev. B **88**, 134403 (2013).
- ⁵⁸ M. Matsumoto and T. Nishimura, ACM Trans. Model. Comput. Simul. **8**, 3 (1998).
- ⁵⁹ “Spirit spin simulation framework (see spirit-code.github.io),” .
- ⁶⁰ J. F. DiTusa, S. B. Zhang, K. Yamaura, Y. Xiong, J. C. Prestigiacomo, B. W. Fulfer, P. W. Adams, M. I. Brickson, D. A. Browne, C. Capan, Z. Fisk, and J. Y. Chan, Physical Review B **90**, 144404 (2014).
- ⁶¹ V. Dyadkin, S. Grigoriev, S. V. Ovsyannikov, E. Bykova, L. Dubrovinsky, A. Tsvyashchenko, L. Fomicheva, and D. Chernyshov, Acta Crystallographica Section B **70**, 676 (2014).
- ⁶² U. K. Rler, Journal of Physics: Conference Series **391**, 012104 (2012).
- ⁶³ A. O. Leonov and M. Mostovoy, Nature Communications **6**, 8275 (2015).
- ⁶⁴ S. Brinker, M. dos Santos Dias, and S. Lounis, arXiv e-prints , arXiv:1902.08607 (2019), arXiv:1902.08607 [cond-mat.mes-hall].
- ⁶⁵ S. Grytsiuk, J. P. Hanke, M. Hoffmann, J. Bouaziz, O. Gomonay, G. Bihlmayer, S. Lounis, Y. Mokrousov, and S. Blügel, arXiv e-prints , arXiv:1904.02369 (2019), arXiv:1904.02369 [cond-mat.mes-hall].
- ⁶⁶ E. Feldtkeller, IEEE Transactions on Magnetism **53**, 1 (2017).
- ⁶⁷ H. Choi, Y.-Y. Tai, and J.-X. Zhu, Phys. Rev. B **99**, 134437 (2019).
- ⁶⁸ M. J. Stolt, X. Sigelko, N. Mathur, and S. Jin, Chemistry of Materials **30**, 1146 (2018).

Appendix A: Connection between Atomistic and Micromagnetic Model in B20 Materials

The atomistic model parameters, which appear in the well-known Heisenberg model, can be connected to the micromagnetic model, that has the form of a continuum theory. The latter is widely used in the skyrmion community and we adopt it to complement our toolbox for the investigation of the magnetic properties of B20-MnGe. We exemplify the connection between atomistic and continuum model by considering a helical spin spiral that points along the z-axis (c.f. 1Q state in eq. (5)) and is described by the wave vector $\vec{q} = (0, 0, q)$, i.e. the magnetic moments rotate within the x-y-plane and the wave vector points along the z-axis. The magnetization of each atom i is then given by

$$\vec{m}_i = \cos(qz_i)\hat{e}_x - \sin(qz_i)\hat{e}_y, \quad (\text{A1})$$

where z_i denotes the z-coordinate of the respective atomic site. It can be shown that such a magnetic struc-

ture interpolates smoothly between the discrete lattice and the continuum limit. We define the Heisenberg energy with isotropic exchange interaction and DM interaction as

$$E_{\text{atom}} = - \sum_{ij} J_{ij} \vec{m}_i \vec{m}_j + \sum_{ij} \vec{D}_{ij} \cdot (\vec{m}_i \times \vec{m}_j). \quad (\text{A2})$$

Insertion of eq. (A1) and usage of addition theorems leads to

$$\begin{aligned} E_{\text{atom,1Q}} &= - \sum_{ij} J_{ij} \cos(q(z_i - z_j)) \\ &+ \sum_{ij} D_{ij}^z \sin(q(z_i - z_j)) \\ &= N(-J(q) + D^z(q)), \end{aligned} \quad (\text{A3})$$

where we used the translational invariance of J_{ij} and N is the number of atoms. For the helical spiral defined in eq. (A1), only the z-component D_{ij}^z of \vec{D}_{ij} needs to be considered.

The micromagnetic energy reads

$$\begin{aligned} E_{\text{micro}} &= \int dV A ((\nabla m_x)^2 + (\nabla m_y)^2 + (\nabla m_z)^2) \\ &+ D \vec{m} \cdot (\nabla \times \vec{m}), \end{aligned} \quad (\text{A4})$$

where A is the so-called *spin stiffness* and D the *DM spiralization*⁴. Insertion of the magnetization of the helical spiral given by eq. (A1) yields

$$\begin{aligned} E_{\text{micro,1Q}} &= \int dV \left[Aq^2 + D (\cos(qz)\hat{e}_x - \sin(qz)\hat{e}_y) \cdot \left(\frac{\partial}{\partial z} \sin(qz)\hat{e}_x + \frac{\partial}{\partial z} \cos(qz)\hat{e}_y \right) \right] \\ &= Aq^2 + Dq. \end{aligned} \quad (\text{A5})$$

The wave number q will take the value which minimizes $E_{\text{micro,1Q}}$ and we can thus impose the condition

$$\frac{\partial E_{\text{micro,1Q}}}{\partial q} \stackrel{!}{=} 0 \Leftrightarrow q = -\frac{D}{2A}, \quad (\text{A6})$$

which gives us a provision on how the wave number q depends on the magnitude of DM spiralization and spin stiffness.

The atomistic and the micromagnetic model are connected in the limit $q \rightarrow 0$, i.e. for a helical spiral that extends over multiple unit cells. Equation (A3) can then

be simplified to

$$\begin{aligned}
E_{\text{atom,1Q}} &= - \sum_{ij} J_{ij} \cos(q(z_i - z_j)) + \sum_{ij} D_{ij}^z \sin(q(z_i - z_j)) \\
&= - \sum_{ij} J_{ij} \left(1 - \frac{1}{2} (q(z_i - z_j))^2 \right) \\
&\quad + \sum_{ij} D_{ij}^z q(z_i - z_j) + \mathcal{O}(q^3) \\
&= - \underbrace{\sum_{ij} J_{ij}}_{E_0} + \frac{1}{2} \underbrace{\sum_{ij} J_{ij} (z_i - z_j)^2}_{A} q^2 \\
&\quad + \underbrace{\sum_{ij} D_{ij}^z (z_i - z_j)}_D q + \mathcal{O}(q^3). \tag{A7}
\end{aligned}$$

Thus in this limit, it is possible to derive the micromagnetic parameters A and D from the atomistic parameters J_{ij} and \vec{D}_{ij} which can be obtained from a KKR calculation by following the procedure described in^{51–53}. The term E_0 determines the ferromagnetic reference energy. The exchange stiffness A describes the increase in energy if a spin spiral is assumed instead of the ferromagnet. The micromagnetic DMI D can lower the energy if the

product of D and q is negative and can thus make the spin spiral configuration the energetically preferred state. In general, A and D are 3×3 tensors that we denote with \mathcal{A} and \mathcal{D} . For B20 compounds this simplifies to diagonal matrices due to symmetry arguments and we obtain

$$\begin{aligned}
\mathcal{A} &= \frac{1}{4} \sum_s J_s \begin{pmatrix} 4\vec{R}_s \cdot \vec{R}_s & 0 & 0 \\ 0 & 4\vec{R}_s \cdot \vec{R}_s & 0 \\ 0 & 0 & \vec{R}_s \cdot \vec{R}_s \end{pmatrix} \\
&= \sum_s J_s \left| \vec{R}_s \right|^2 \underline{\underline{I}}_3 = A \underline{\underline{I}}_3 \tag{A8}
\end{aligned}$$

and

$$\begin{aligned}
\mathcal{D} &= \frac{1}{2} \sum_s \begin{pmatrix} 4\vec{R}_s \cdot \vec{D}_s & 0 & 0 \\ 0 & 4\vec{R}_s \cdot \vec{D}_s & 0 \\ 0 & 0 & 4\vec{R}_s \cdot \vec{D}_s \end{pmatrix} \\
&= 2 \sum_s \left(\vec{R}_s \cdot \vec{D}_s \right) \underline{\underline{I}}_3 = D \underline{\underline{I}}_3. \tag{A9}
\end{aligned}$$

Here, the summation is performed over all shells s , so that symmetrically equivalent parameters are omitted. It should be noted that from eq. (A9) it follows that D vanishes for $\vec{D}_n \perp \vec{R}^n$ and is largest for $\vec{D}_n \parallel \vec{R}^n$.